Modeling of microstructural effects on the creep of hardened cement paste using an experimentally informed lattice model

Gan, Yidong; Romero Rodriguez, Claudia; Zhang, Hongzhi; Schlangen, Erik; van Breugel, Klaas; Šavija, Branko

DOI
10.1111/mice.12659

Publication date
2021

Document Version
Final published version

Published in
Computer-Aided Civil and Infrastructure Engineering

Citation (APA)
Gan, Y., Romero Rodriguez, C., Zhang, H., Schlangen, E., van Breugel, K., & Šavija, B. (2021). Modeling of microstructural effects on the creep of hardened cement paste using an experimentally informed lattice model. *Computer-Aided Civil and Infrastructure Engineering*, *36*(5), 560-576. https://doi.org/10.1111/mice.12659

DOI: 10.1111/mice.12659

ORIGINAL ARTICLE

COMPUTER-AIDED CIVIL AND INFRASTRUCTURE ENGINEERING WILEY

Modeling of microstructural effects on the creep of hardened cement paste using an experimentally informed lattice model

Yidong Gan[1] | **Claudia Romero Rodriguez**[1] | **Hongzhi Zhang**[2] | **Erik Schlangen**[1] | **Klaas van Breugel**[1] | **Branko Šavija**[1]

[1] Faculty of Civil Engineering and Geosciences, Delft University of Technology, Delft, The Netherlands

[2] School of Qilu Transportation, Shandong University, Jinan, PR China

Correspondence
Branko Šavija, Faculty of Civil Engineering and Geosciences, Delft University of Technology, 2628 CN Delft, The Netherlands.
Email: b.savija@tudelft.nl

Funding information
China Scholarship Council, Grant/Award Number: 201706130140; Construction Technology Research Program, Grant/Award Number: 17SCIP-B103706-03; Taishan Scholar Foundation of Shandong Province, Grant/Award Number: tsqn201909032

Abstract

This paper presents a method to numerically investigate the microstructural effect on the creep behavior of cement paste at the microscale. The lattice fracture model is extended to consider local time-dependent deformations of calcium-silicate-hydrate phases in the cement paste by imposing local forces. The term "experimentally informed model" is used herein as the heterogeneous microstructures of hardened cement pastes were obtained by using the X-ray computed microtomography and directly implemented into the model. The mechanical and creep properties of different constituents at the resolution of 5 μm were inversely identified from the fracture and creep bending tests on cementitious microcantilever beams at the microscale. The model is then validated through the comparison with the testing results of cement pastes with different *w*/*c* ratios and microstructures. It is found that the developed model can successfully reproduce experimentally observed behaviors and be applied to explain the experimental results in detail. With the method presented in this paper, the relationship between the volume fractions of different components and the global creep behavior of cement paste can be established. The validation of the model performed at the microscale forms a basis for the multiscale analysis of concrete creep.

1 | INTRODUCTION

Creep may impair the durability of a concrete structure in several aspects, such as loss of prestress in concrete members and excessive deflections of concrete bridges (Bažant, Hubler, & Yu, 2011; Beltempo, Bursi, Cappello, Zonta, & Zingales, 2018). Creep can also be beneficial, for example, by reducing the shrinkage-induced stresses at early ages (Gawin, Pesavento, & Schrefler, 2006). Despite decades of research, it is still a great challenge to accurately predict the creep of concrete. One of the main reasons for this difficulty can be attributed to the multiscale heterogeneous nature of cementitious materials. At the macroscale or structural level, concrete is usually assumed to be homogeneous and isotropic, which facilitates the creep analysis of concrete structures. At the mesoscale, concrete is considered to be a composite material, which mainly comprises cement paste, aggregate, and interfacial transition zone (ITZ). The cement paste, which is the main creeping phase in concrete, can be further broken down into

multiple phases at the microscale, such as unhydrated cement (UHC) grain, capillary pores, and hydration products. Moreover, it has long been recognized that there are mainly two types of calcium–silicate–hydrate (C–S–H) in cement paste at the microscale (Constantinides & Ulm, 2004). When it comes to the nanoscale, the colloidal C–S–H particles are generally considered as the "basic building blocks," which are also recognized as the origin of creep (Jones & Grasley, 2011; Suwanmaneechot, Aili, & Maruyama, 2020; Vandamme & Ulm, 2013). It is clear that a reliable and accurate prediction model for concrete creep needs to account for the multiscale character of the cementitious material (Granger & Bažant, 1995; Honorio, Bary, & Benboudjema, 2016). This requires the development of a multiscale modeling scheme to connect the heterogeneous material structures and properties at finer scales to the macroscopic creep behavior (Havlásek & Jirásek, 2016). However, most existing creep models are either entirely empirical or based on mathematical functions that fit the macroscopic experimental data (Rahimi-Aghdam, Bažant, & Cusatis, 2019; Šmilauer & Bažant, 2010). The complex material structure is not considered in these models. It is therefore difficult for them to give accurate prediction of creep deformation. Moreover, these models are unable to extrapolate creep behavior of new modified concrete mixtures or guide the performance-oriented optimization of the macroscopic creep properties.

Recently, several efforts have been made in the context of multiscale modeling of creep. At the mesoscale, Giorla and Dunant (2018) investigated the effect of mesostructure of concrete on the macroscopic creep using finite-element simulations (FEM). Their findings indicate that the shape and orientation of aggregate particles might induce anisotropy in the macroscopic creep behavior, and that finer particles appear to reduce the macroscopic creep when the volume fraction of the aggregate is kept the same. Similarly, the numerical study conducted in (Lavergne, Sab, Sanahuja, Bornert, & Toulemonde, 2015) suggests that the ITZ largely affects the creep of concrete. At the microscale, Li, Grasley, Garboczi, and Bullard (2015) used FEM simulation combined with the computer-generated microstructure to study the viscoelastic behavior of hydrating cement paste at early age. The simulation results suggest that the time-dependent dissolution of cement grains should be considered as a significant mechanism for the early-age creep of cement paste. For mature cement paste, microstructural simulations have been carried out by Z. Hu et al. (2019) to study the effects of material compositions on the basic creep of cement paste. However, simplified microstructures with idealized circular inclusions were used in their simulations. It has to be emphasized that, to improve the accuracy of the multiscale model, two major conditions should be fulfilled. The first one is to implement a (more) realistic material structure into the model. To the best of the authors' knowledge, there have been no published studies directly linking real cementitious microstructures to macroscopic creeps. Models published in the past are mainly based on numerical or analytical homogenization, such as Mori–Tanaka method (Königsberger, Irfan-ul-Hassan, Pichler, & Hellmich, 2016; B. Pichler & Hellmich, 2011), and start from an idealized microstructure. Another condition is to validate the model using experimental data at every scale. As there is always a scale gap between the laboratory-sized samples and the characteristic size of representative volume element of cement paste (around several hundreds of micrometers), the validation of model at the microscale is still a difficult task.

Owing to the recent development of experimental characterization techniques in Gan et al. (2020), we now focus on developing and validating a short-term creep model at the microscale, which considers the microstructure of cement paste and micromechanical and viscoelastic properties of different constituents. With the validated model, it would be possible to predict the short-term creep of any cement paste if given the microstructure. This would also be helpful in the case of predicting the early age creep, which is difficult to measure experimentally. To the best of the authors' knowledge, this is the first attempt to develop and directly validate such a creep model at the microscale using experimental data, which are obtained at the same scale. This is also an essential starting point in the development of multiscale modeling scheme for predicting the creep of concrete structure.

Generally, the heterogeneous microstructure of cement paste can be obtained by either experimental techniques, for example, scanning electron microscopy and X-ray computed microtomography (XCT) (H. Zhang, Šavija, Figueiredo, Lukovic, & Schlangen, 2016; H. Zhang, Šavija, Figueiredo, & Schlangen, 2017), or computer-generated methods, for example, HYMOSTRUC (Van Breugel, 1993), μic (Bishnoi & Scrivener, 2009), and CEMHYD3D (Bentz, 2006). In pursuit of a realistic microstructure, experimental techniques are always favored. For the identification of mechanical and viscoelastic properties of individual constituents in cement paste, the microstructural inverse analysis is commonly used to downscale from experimental data of cement paste or concrete at larger scale (Z. Hu et al., 2019; Königsberger et al., 2016; C. Pichler & Lackner, 2009; Šmilauer & Bažant, 2010). In this study, an inverse analysis method was adopted to identify the local creep properties for different constituents at the resolution of 5 μm. Alternative identification methods through the direct measurements on individual phases, such as nanoindentation tests and universal testing at finer scale, may also be possible (Shahrin & Bobko, 2019; Vandamme

& Ulm, 2013). However, there has been no published work on the finer scale creep test yet. It should also be noted that although the nanoindentation technique is an important tool for accessing long-term creep properties of C–S–H (Vandamme & Ulm, 2009), the short-term creep behavior may not be appropriately characterized due to the very large stress arising in the probed volume by the indentation tip (Yu et al., 2018).

For the creep analysis within the service stress range, it is generally assumed that the creep of cementitious material obeys the principle of superposition and may be formulated in terms of hereditary integrals (Bažant, 1971). In the framework of linear viscoelasticity, the calculation of creep deformation under variable stress can be greatly facilitated by using this principle. Sassone and Casalegno (2012) proposed an integral-type computational approach for the analysis of concrete creep based on the coupling of the finite-element method with a numerical solution of the hereditary Volterra integral equations. The viscoelastic problem is solved incrementally as a sequence of elastic analyses, in which the elastic modulus is updated and the effect of the stress history is considered at each step based on previous solution results. The numerical computation of this type of integral can be achieved by replacing the hereditary integral with a finite sum using the trapezoidal rule, as suggested in Bažant (1971, 1972). However, for general applications in finite-element programs, the numerical integration requires the storage of the entire stress history at each integration point of each finite element (Bažant, 1988). As a result, the evaluation of the integral requires an extensive memory capacity and a progressively increasing number of calculations for each time step (Bažant, 1988; Di Luzio, Cedolin, & Beltrami, 2020). In the literature, several simplified and approximate methods for the calculation of creep strain have also been adopted, such as the aging coefficient method (Bažant, 1972; Granata, Margiotta, & Arici, 2013) and the parallel creep method (Park, Lee, & Lee, 2016). In addition, it is suggested in Bažant (1988) that the computational cost can be substantially reduced if the integral-type constitutive equations are replaced by the differential-type laws. This can be achieved through the approximation of the compliance function by a Dirichlet series corresponding to a Kelvin rheological chain that can be integrated in a step-by-step manner (Bažant, 1988; Šmilauer & Bažant, 2010). This computational approach only needs to store a limited number of hidden variables instead of the entire loading history (Bažant, 1988; Di Luzio et al., 2020). It is worth mentioning that the Dirichlet series expansion should be considered only as an approximation to the real compliance function, rather than a fundamental law.

For both integral and differential creep functions, it has been demonstrated that the numerical step-by-step creep analysis can be reduced to a sequence of elastic finite element analyses (Bažant, 1972, 1988; Di Luzio et al., 2020). Following this idea, a different numerical algorithm using power-law creep functions is developed in the current study. Herein, the creep analysis is carried out by solving a sequence of fictitious elastic problems with imposed local forces. Note that different applications may affect the choice of computation algorithm. Some creep models for different applications and external conditions have been developed in the literature (Bažant, 1972; Giorla & Dunant, 2018; Sassone & Casalegno, 2012; Šmilauer & Bažant, 2010). They differ in their practical purpose, degree of accuracy, and simplicity. As the focus of current study is to simulate the microstructural effect on the short-term creep behavior of hardened cement paste subjected to constant loading, the computational aspect related to the complicated stress history solutions may not play a dominant role.

Regarding the numerical technique, a lattice-type model is used herein to simulate the creep of cement paste. Lattice models have been widely used for simulating the fracture process, moisture transport, and chloride diffusion of cement-based materials (Bolander & Berton, 2004; Lilliu & van Mier, 2003; Luković, Šavija, Schlangen, Ye, & van Breugel, 2016; Qian, 2012; Šavija, Luković, & Schlangen, 2014; Yip, Mohle, & Bolander, 2005, 2019 H. Zhang, Šavija, Luković, & Schlangen, 2019). The extension of the lattice model to consider the time-dependent deformation is conducted in this study. The main advantage of the lattice model is that it allows a straightforward implementation of the complex material heterogeneity in the model, while using simple constitutive laws for local elements with only a few fitting parameters (Luković et al., 2016; Šavija et al., 2014; H. Zhang et al., 2016). Therefore, the lattice-type model offers an excellent opportunity to investigate the influence of microstructure on the creep of cement paste. Moreover, it has been reported that the creep behavior is closely related to the density of microcracks created during the loading phase (Rossi, Tailhan, Le Maou, Gaillet, & Martin, 2012). Therefore, the lattice model, which is a sophisticated computational tool in fracture analysis, may have the potential to predict the time-dependent deformation behavior associated with the microcracking.

In this study, the virtual specimens containing heterogeneous microstructures were first generated based on the XCT results of cementitious microcantilever beams. The local mechanical and creep properties for different constituents in cement paste were then identified based on the microscale fracture and creep testing results obtained in Gan et al. (2020). After the local properties were identified, the fracture and creep simulations were separately carried

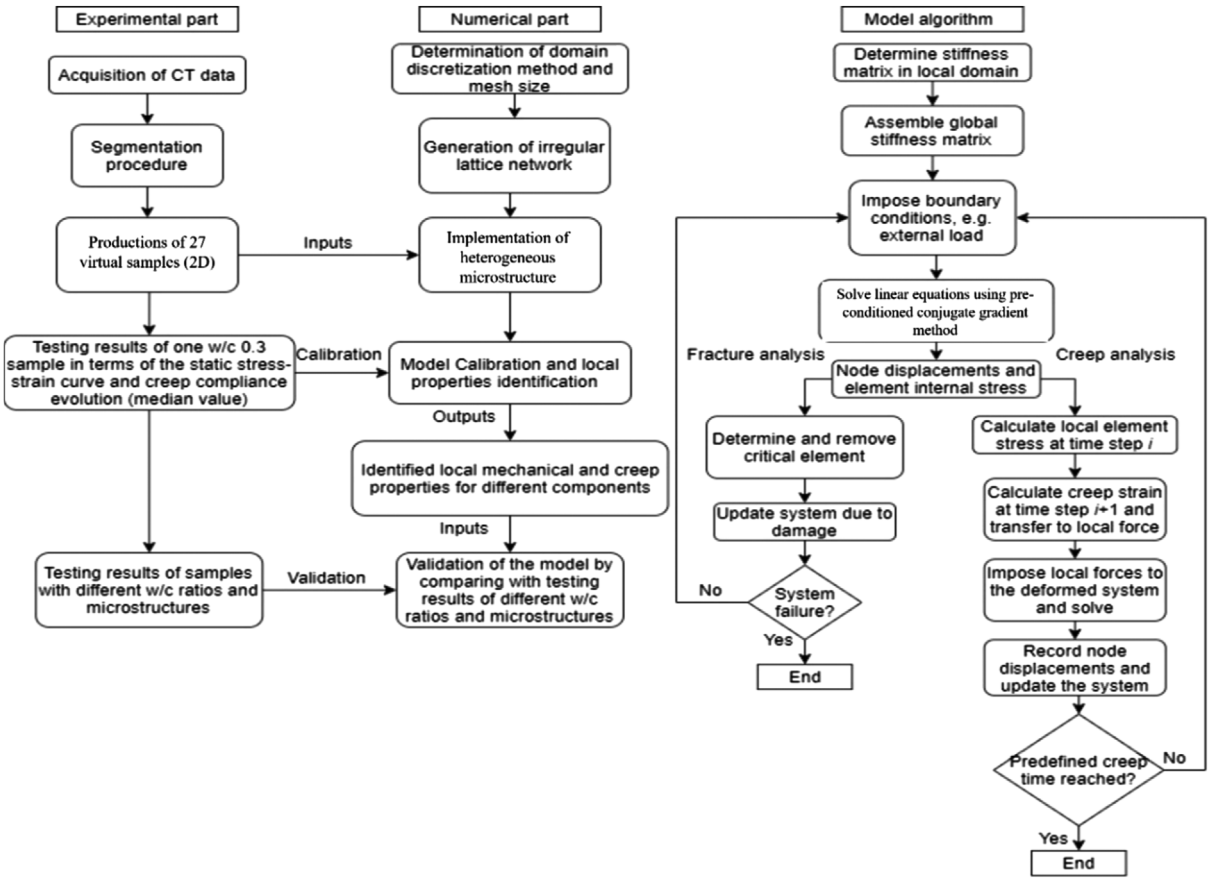

FIGURE 1 The organization of the current paper

out on these virtual specimens. The relationships between the global mechanical and creep properties were compared with experimental observations. The microstructural effects on the global creep deformation were also investigated using the developed model. The organization of the current paper is presented in Figure 1. It must be noted here that the current model is limited to simulating the short-term creep behavior of cement paste, of which the microstructure is time-invariant and the creep is assumed to originate from the main hydration product (C–S–H). The investigations on the evolution of microstructure and more complex coupling mechanisms are beyond the scope of the current paper.

2 | METHODOLOGY

2.1 | 2D virtual specimen

2.1.1 | Acquisition of CT scans

Microcantilever beams were fabricated to obtain the realistic microstructure of cement paste at the microscale. The cement paste was prepared with standard grade CEM I 42.5 N Portland cement and deionized water. Three water-to-cement (w/c) ratios (0.3, 0.4, and 0.5) were used. After sealed curing for 28 days, the cement paste was then cut by a precision microdicing machine (MicroAce Series 3 Dicing Saw) to generate microcantilever beams with a square cross section of 300 μm × 300 μm. The cantilevered length of the beam is around 1,650 μm. For the details regarding the preparation process of microcantilever beams, the reader is referred to previous works of the authors (Gan et al., 2020; Gan, Zhang, Šavija, Schlangen, & van Breugel, 2018). The prepared beams were then scanned using X-ray computed tomography (XCT) to obtain gray scale images of beams containing the information of heterogeneous microstructure. Basically, the XCT images record the difference in X-ray linear attenuation coefficients by means of the gray value, which fundamentally depends on the density of the material. For each w/c ratio, three beams were scanned. Figure 2 shows the cantilever beams fixed on the glass holders that can be clamped by the rotatable stage of the CT scanner. The X-ray source tube was set at 110 kV/100 μA during scanning. The obtained voxel resolution is 1 μm × 1 μm × 1 μm. In addition, extra beams with different w/c ratios were scanned with higher resolution, that is, 0.5 μm × 0.5 μm × 0.5 μm, to determine the total

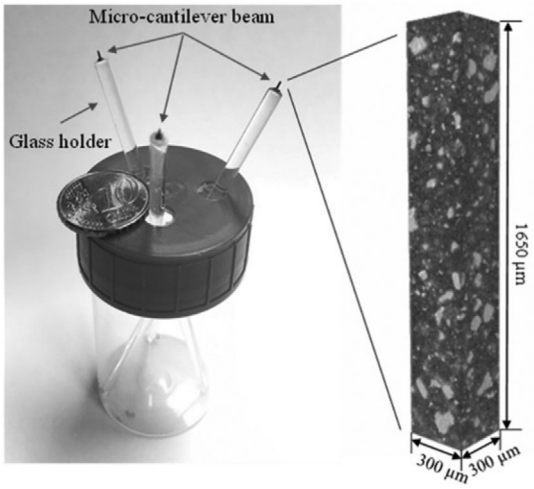

FIGURE 2 The CT scanning of the microcantilever beams

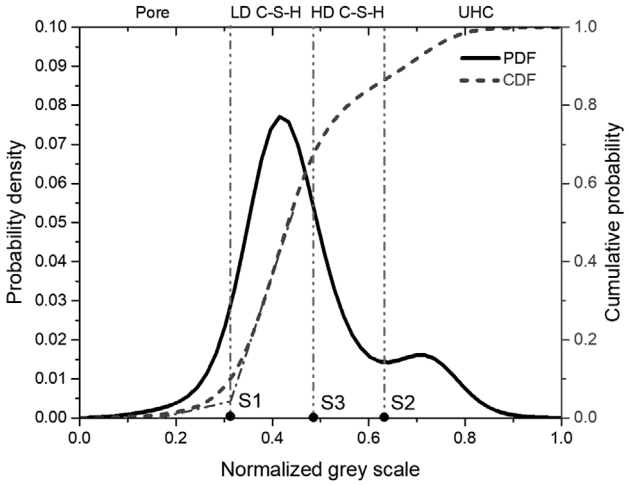

FIGURE 3 Image segmentation through gray scale histogram of CT images

porosity. The obtained porosity for w/c 0.3, 0.4, and 0.5 are 4.39% ± 0.19%, 7.40% ± 0.43%, and 12.06% ± 0.75%, respectively. Note that due to the limitation of image resolution in XCT, pores smaller than 0.5 μm cannot be detected and are mixed within the segmented solid phases. Therefore, the porosity measured by XCT (mainly capillary pores) is, in general, much lower than the porosity measured by the mercury intrusion porosimetry (Ye, 2003). Nevertheless, the differences in porosity for different w/c ratios have been clearly demonstrated.

The second step is to distinguish different phases based on the gray scale values of CT images. In this study, a global thresholding method is adopted (Wong, Head, & Buenfeld, 2006; M. Zhang, He, Ye, Lange, & van Breugel, 2012; H. Zhang et al., 2016). As shown in Figure 3, three threshold values are defined to segment pores, UHC, high-density (HD) C–S–H, and low-density (LD) C–S–H based on the gray scale histogram. Note that calcium hydroxide (CH), ettringite (AFt), and monosulfate (AFm) are difficult to be segmented based on the CT scans due to similar density. As a result, they are embedded in other segmented hydration products. A brief description of the segmentation approach is provided: the inflection of the cumulative curve was defined as the upper threshold value for pores (S1) as shown in Figure 3. This value refers to the critical point where the segmented pore areas start to overflow to the surrounding paste (Wong et al., 2006). The gray scale value corresponding to a change of the tangent slope was used as the lower threshold level for UHC (S2); the threshold value for LD/HD C–S–H was selected according to the model proposed by Tennis and Jennings (2000). A key element of this model is a division of C–S–H into two types, each with a specific density. In this model, the degree of hydration α and w/c ratio are used as input:

$$M_r = 3.017\,(w/c)\,\alpha - 1.347\alpha + 0.538 \quad (1)$$

where M_r is the ratio of the mass of LD C–S–H to the total mass of C–S–H; the degree of hydration α was estimated using the following equation:

$$\alpha = \frac{V_h/\upsilon}{V_h/\upsilon + V_u} \quad (2)$$

where V_h and V_u denote volume fractions of hydration products and UHC grains, respectively; υ is the volume reaction product/volume reactant ratio and assumed as 2.2 (Van Breugel, 1993). By assuming the density of LD C–S–H and HD C–S–H as 1,440 and 1,750 kg/m^3, respectively, the volume fractions of LD and HD C–S–H and the corresponding threshold value (S3) can be determined (Tennis & Jennings, 2000). Note that all the segmentation processes are based on the 3D CT results with the resolution of 1 μm/voxel. It needs to be clarified that using the global threshold values to distinguish different phases based on the gray scale histogram can never be a perfect approach. With many segmentation methods available in the literature, it is difficult, if not impossible, to assess which segmentation method produces the most accurate threshold value (Wong et al., 2006). When comparing results with other methods for segmentation, the different assumptions and inherent limitations of these techniques have to be considered.

2.1.2 | Generation of 2D virtual specimens

For each w/c ratio, nine virtual specimens (2D) were generated using random slices extracted from the XCT results.

TABLE 1 Details of segmented microstructures of virtual specimens with different *w/c* ratios

w/c	Porosity (%)	$R_{LD/HD}$	α (%)
0.3	2.77 ± 0.59	0.25 ± 0.07	75.35 ± 3.18
0.4	4.29 ± 1.11	0.76 ± 0.18	80.57 ± 4.69
0.5	5.41 ± 1.78	2.68 ± 0.24	86.34 ± 3.44

In total 27 virtual 2D specimens were used for the generation of microstructure informed lattice structures. Moreover, a trade-off has been made by reducing the resolution to 5 μm/pixel in order to save computational time and, at the same time, reserve primary information of local structure. Based on the previously described segmentation procedure, the porosity, volume fraction ratio between LD and HD C–S–H ($R_{LD/HD}$) and degree of hydration (α) for three *w/c* ratios are listed in Table 1. The number after ± indicates the standard deviation. It should be noted again that due to the resolution (5 μm/pixel) used here for the simulations, the microstructure information at lower scale is not included.

2.2 | Lattice model description

In this study, the 2D lattice model is extended to investigate the creep behavior of cement paste. It has to be noted that the 2D analysis is a strong idealization of the responses of 3D beams subjected to bending. In this study, the properties at the third direction are assumed to be constant and the in-plane displacements, strains, and stresses are also assumed to be uniform through the thickness of the beam. The first step of modeling is to generate the 2D lattice structure. A group of cells is generated based on the pixel images and each cell coincides with a single pixel. In each pixel, a subcell is created and the length ratio of the subcell to the cell is here set as 0.5 (H. Zhang, Šavija, & Schlangen, 2018). The centers of cells and subcells are coincident. Subsequently, a node is randomly created inside each subcell. This is achieved by using a pseudo-random number generator to determine the node coordinates at *X*-axis and *Y*-axis, respectively. Each coordinate is created following a uniform distribution. Delaunay triangulation is then performed on these nodes as described in Šavija et al. (2014) and Yip et al. (2005). In this way, the neighboring nodes are connected to form the lattice network, as shown in Figure 4. The major reason for using irregular lattice models with random nodes is to introduce local heterogeneity and disorder (Schlangen & Garboczi, 1997). The total number of beam elements is 34,493. Finally, the heterogeneous microstructure of the material can be explicitly considered by assigning these beams with different properties. Figure 5 shows the generated typical lattice models for different *w/c* ratio based on the segmented 2D virtual specimens. Note that for the interface elements between two different phases, the lower mechanical and creep properties among these two phases were assigned.

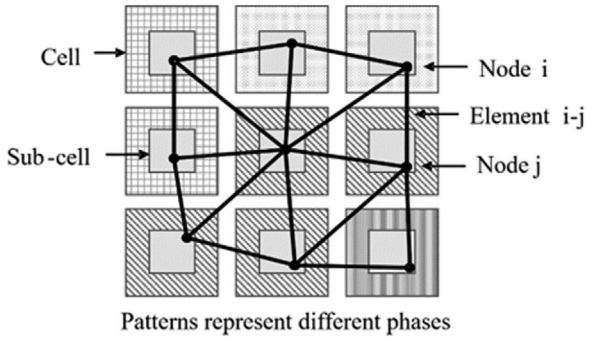

FIGURE 4 Lattice element generation procedure

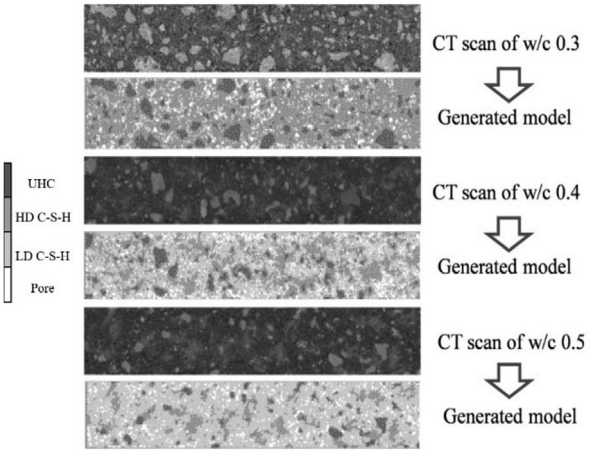

FIGURE 5 Segmentation results for different *w/c* ratios

Before performing the creep simulation, the local mechanical properties of individual phases, in terms of fracture strength and elastic modulus, should be identified first. Therefore, the fracture analyses of these virtual specimens were conducted before the creep simulations. It should be addressed here that several differences in 2D and 3D fracture simulations can be expected. For instance, the realistic 3D connectivity and tortuosity of pore structure, which largely affect the crack pattern, cannot be considered in 2D simulations. Consequently, there is a reduction in fracture energy in 2D compared to 3D simulations. Moreover, Huang, Yan, Yang, and Liu (2016) reported that the 3D model has a higher modulus (around 5.6%) than the 2D models, which fail to simulate out-of-plane interlock effects of stiff inclusions. In contrast, the simulations conducted by Luković, Schlangen, and Ye (2015) suggested that 2D and 3D simulations of cementitious materials may generate similar average prepeak behaviors. These small differences of elastic behaviors in 2D and 3D simulations

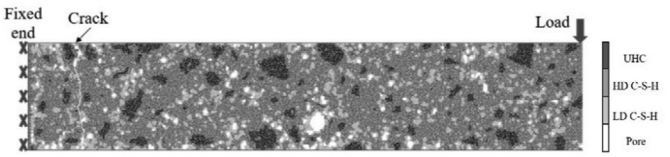

FIGURE 6 The boundary conditions of the model and the fractured patterns for *w*/*c* 0.3 specimen under bending load

may lend support to the possibility of using a 2D model to interpret the 3D elastic deformation measurements. For the creep simulation, several studies have argued that the validity of using the 2D model as simplification of 3D elastic behavior may also hold for the viscoelastic behavior, especially when the connectivity of viscoelastic phase (C–S–H matrix) is preserved in the 2D model and the volume of the elastic inclusions is relatively low (Giorla & Dunant, 2018; Z. Hu et al., 2019). Nevertheless, it is always critical and necessary to use the 3D models to reproduce the experimental results, which are always in 3D. The 2D model is favored in this study mainly due to its numerical convenience and computational efficiency.

In the fracture simulations, all beam elements (Timoshenko beams) are assumed to exhibit linear elastic behavior and have constant Poisson's ratio of 0.2. The same boundary condition of microcantilever beam bending test is used, as shown in Figure 6: one short side of the virtual specimen is fixed and a vertical load is applied at the free end of beam. Under the imposed external boundary condition, the stress of each element is calculated. At each loading step, the critical element with the highest stress/strength ratio is removed from the mesh. The analysis procedure is then repeated until a predetermined failure criterion is achieved. In this case, the maximum stress criterion is used. For the calculation of fracture stress σ_f, both normal force and bending moment are taken into consideration by the following general relation (Schlangen & van Mier, 1992; H. Zhang et al., 2017):

$$\sigma_f = \alpha_N \frac{N}{A} + \alpha_M \frac{M}{W} \tag{3}$$

where A denotes the cross-section area of the beam element; W is the cross-sectional moment of resistance; N and M are the local normal force and bending moment, respectively. α_N and α_M represent the normal force influence factor and the bending influence factor. Their values are generally adopted as 1.0 and 0.05, respectively (Qian, 2012; Šavija, Zhang, & Schlangen, 2020).

For the simulation of short-term creep behavior, only the beam elements belonging to LD C–S–H and HD C–S–H phases are assumed to creep under loading. It is worth mentioning that the hydrodynamic relaxation caused by the presence and movement of free water in the saturated pores may also contribute to the time-dependent deformation (Alizadeh, Beaudoin, & Raki, 2010; Mallick, Anoop, & Balaji Rao, 2019; Vichit-Vadakan & Scherer, 2003; Wittmann, 1982). However, because the model is calibrated on samples with little free water in the capillary pores, the creep deformation related to the movement of capillary water and the change of capillary pressure are not considered. It is also assumed that the viscoelastic behavior of C–S–H phases mainly depends on the presence of gel and interlayer water at the nanoscale (Bažant, Hauggaard, Baweja, & Ulm, 1997; Suwanmaneechot et al., 2020; Tamtsia & Beaudoin, 2000). At the first step of creep simulation, a predefined constant load (30% of maximum load in this study) is applied on the specimen. The initial local stresses in all lattice beams are calculated and beams that meet the fracture criterion are removed from the original mesh to consider the initial damage. The stress is then redistributed to other solid phases. Note that the microcracking analysis using maximum stress criterion is only applied during the loading stage where the external load is increased from zero to the constant load. In the following creep steps, the microcracking is assumed to be not involved as low stress level is applied. This is also in accordance with the experimental observations (Gan et al., 2020). Note that the situation would be different for young concretes at early age, where further damage involved during the creep stage may play an important role.

For the creep constitutive law of C–S–H, Bažant and Prasannan (1989) introduced a log-power function to describe the "intrinsic" creep compliance function of nonaging cement gel. The log-power function evolves asymptotically as a power function of load duration for short time and evolves asymptotically as a logarithmic function for long time (Bažant et al., 1997; Di Luzio et al., 2020; Granger & Bažant, 1995; Šmilauer & Bažant, 2010). This is based on the experimental observations that the creep curves of cement paste and concrete exhibit two distinct kinetics depending on the loading duration (Gan et al., 2020; Vandamme & Ulm, 2013; Q. Zhang, Le Roy, Vandamme, & Zuber, 2014). As the elastic restraint of noncreeping phases, for example, UHC grain and CH, does not significantly affect the time evolution of creep curves, the compliance functions of C–S–H and of cement paste are expected to be similar (Šmilauer & Bažant, 2010). Normally, the Dirichlet series approximation is performed to describe the real continuous compliance functions (e.g., power-law function) and transfer them

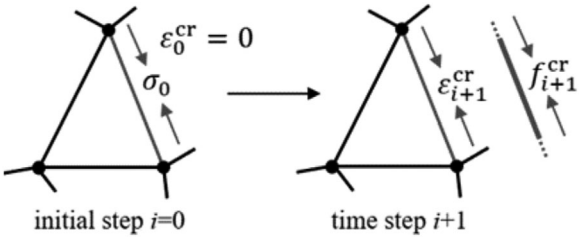

FIGURE 7 Schematic illustration of creep deformation and local axial force in the lattice model

into rate-type laws for the computational convenience (Di Luzio et al., 2020; Yu et al., 2018). However, the Dirichlet series expansion contains unnecessarily many empirical parameters and appropriate identifications of theses parameters are not easy (Bažant, 1988). A creep function with only a few parameters could make the computational analysis straightforward and efficient. For this purpose, the power-law function is assumed and directly applied for modeling the creep of C–S–H in view of the short-term creep considered in this study. The creep compliance function can thus be written as

$$C(t,t_0) = \frac{1}{E_c}\left(\frac{t-t_0}{t_1}\right)^{\beta} \tag{4}$$

where $C(t,t_0)$ is the basic creep compliance of C–S–H at time t; t_0 is the sample age when load is applied and t_1 is the time unit (1 s); E_c is defined as creep modulus, which will be identified by experiments; the exponent β is a constant, which equals to 0.251 in this study (Königsberger et al., 2016). It can be seen from Equation (4) that only the creep modulus of C–S–H phase needs to be identified in the model. For each time step, the incremental creep strain of the beam can be obtained based on Euler's method:

$$\varepsilon_{i+1}^{cr} - \varepsilon_i^{cr} = \frac{1}{E_c} \cdot \beta \cdot \Delta t \cdot \sigma_i \cdot \left(\frac{t-t_0}{t_1}\right)^{\beta-1} \tag{5}$$

The creep strain increment $\varepsilon_{i+1}^{cr} - \varepsilon_i^{cr}$ at $i+1$ step is dependent on the local beam axial stress σ_i and time interval Δt (1 s). The creep strain increment of each beam is then converted into temporary local axial force f_{i+1}^{cr} (Lyu, Schlangen, & van Breugel, 2018). By applying these local axial forces on the deformed lattice model, the local incremental creep strain can be achieved. Note that the creep strain induced by the bending moment has been indirectly considered in Equation (3). Before the next creep step, these local axial forces are relaxed and the deformation of every lattice element is saved. This process is schematically shown in Figure 7. One main advantage of this numerical algorithm is that it can be easily incorporated into any finite-element program. The creep analysis is, therefore, converted to a series of elasticity problems. This is somehow similar to the effective modulus approach reported in Bažant (1972, 1988) except that the local force is updated at each time step in current method instead of the elastic stiffness matrix. In this model, the compressive and tensile creep functions are assumed to be the same for simplicity even though very contradictory findings have been reported in the literature (Forth, 2015; Liang & Wei, 2019; Ranaivomanana, Multon, & Turatsinze, 2013; Rossi, Tailhan, & Le Maou, 2013; Wei, Wu, Huang, & Liang, 2018) and there is no consensus yet on this issue.

The local stresses of beams are updated in every time step by executing another step with only constant loading on the deformed configuration. In this way, the redistribution of stresses is calculated. It is found that the changes of stresses in this model during each time step are very small (<0.005%) due to the very short loading duration (1 s). Note that in reality the internal stresses tend to redistribute from creeping phases to noncreeping phases or newly formed hydration products due to the relaxation of viscous C–S–H interlayer during creep (Sellier et al., 2016; Šmilauer & Bažant, 2010) or dissolution of cement grains (Bažant et al., 1997; Li et al., 2015; Moradian, Ley, & Grasley, 2018). However, in any case, the redistribution of stress may be apparent only for much longer loading duration (Bažant et al., 1997; Granger & Bažant, 1995; Li et al., 2015; Šmilauer & Bažant, 2010). In this model, due to the negligible changes of stresses in the short-term, the superposition procedure of creep strain considering the stress history can thus be simplified by only superimposing the incremental creep strain at each time step. The extension of the model to consider the local stress history under long-term loading is also possible but is not included in current study.

2.3 | Local properties identification

As mentioned in Section 2.2, there are several properties in the fracture model and creep model, which need to be identified based on the microscale tests. The details of fracture and creep bending tests can be found in the author's previous work (Gan et al., 2020). The 28-day-old cement paste specimens were loaded under constant flexural loading in an environment with constant temperature and humidity. The testing results including the static stress–strain curve and specific basic creep compliance evolution for a single sample with the w/c of 0.3 were used here as the benchmark for the identification process. Note that samples with the w/c of 0.3 also have the least scattered experimental results compared to the results of w/c 0.4 and 0.5 samples (Gan et al., 2020). This sample was selected as it has the median basic creep compliance among all the creep tests for w/c 0.3 samples. It is then assumed that both the

mechanical and viscoelastic properties of different phases at the scale of 5 μm are not largely affected by the *w*/*c* ratio, which is in accordance with the conventional nanoindenation results (C. Hu & Li, 2015; Vandamme & Ulm, 2013). Therefore, in the simulation of specimens with the *w*/*c* ratios of 0.4 and 0.5, the same lattice element properties were used. This assumption may also indicate that the microstructure instead of the nanostructure is the critical scale responsible for the global behavior of cement paste (Giorla & Dunant, 2018; Z. Hu et al., 2019; Wyrzykowski, Scrivener, & Lura, 2019). It still should be emphasized here that because a resolution of 5 μm was used, the identified properties of LD C–S–H and HD C–S–H phases are the results of the C–S–H gel mixed with small pores. Although further downscaling to the C–S–H building blocks considering the nanostructure is possible (Z. Hu et al., 2019), it will not be explored here.

For the identification of local mechanical properties (i.e., tensile strength and elastic modulus) of different components, it is mainly based on the conventional nanoindentation tests conducted in C. Hu and Li (2014), which give the information of the local indentation elastic modulus and hardness for different components. As the local tensile strength cannot be directly measured, ratios of tensile strength among each phase are then assumed to be equal to ratios of measured indentation hardness among these phases. Therefore, if the mechanical properties of one single phase are determined by comparing with experimental data, the properties of other phases could be determined (Luković et al., 2015; H. Zhang et al., 2016). For the determination of local creep properties, a constant ratio between the creep modulus of HD C–S–H and LD C–S–H is chosen as 1.481 based on the ratio of contact creep modulus measured in nanoindentation creep tests (Vandamme & Ulm, 2009). The local stress and strain responses at the top surface of the beam near the fixed end are selected to present the results (Gan et al., 2020). The numerical results, in terms of stress–strain curves and the specific basic creep compliance curves, are shown in Figure 8. The specific basic creep compliance is defined as the creep compliance under constant loading at no moisture exchange. For the fracture simulations, the prepeak stage, which is used to determine the global strength and elastic modulus, agrees well with the experiments. Moreover, the model provides the postpeak behavior of cement paste, which could not be experimentally measured due to the limitation of the testing equipment (Gan et al., 2020; H. Zhang, Gan et al., 2019). The zigzag behavior observed in the simulated postpeak stress–strain curve represents the crack formation and propagation progress (Lilliu & van Mier, 2003). As shown in Figure 8b, a good agreement with experimental data is also observed for the creep simulation. It needs to be mentioned

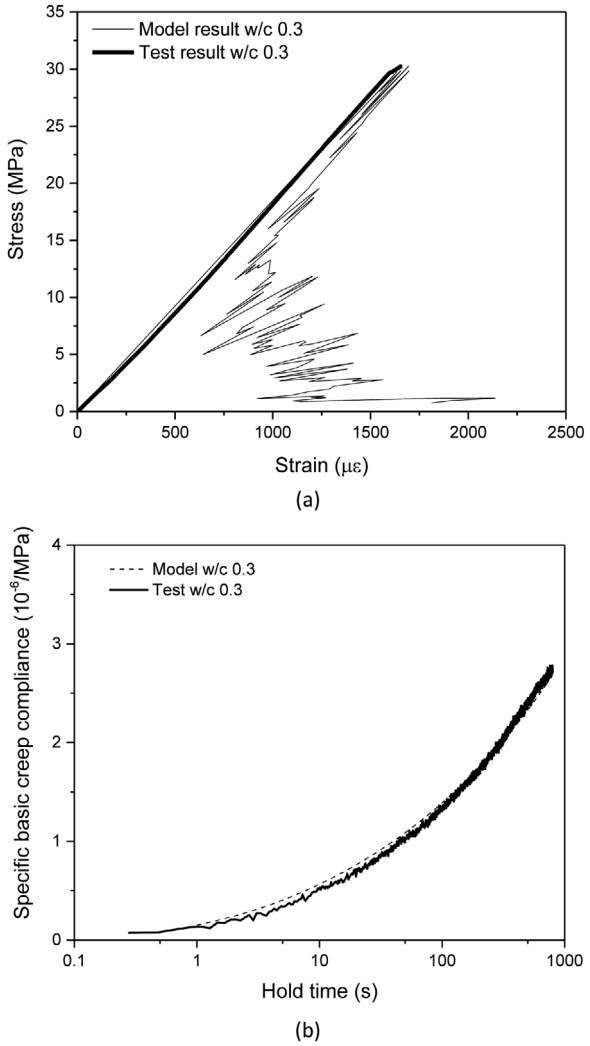

FIGURE 8 The comparisons between the simulations and (a) mechanical properties and (b) creep properties

TABLE 2 The identified local properties for different phases

Phases	f_i (MPa)	E_i (GPa)	C_i ($\times 10^3$ GPa)
UHC	614.7	84.2	–
LD C–S–H	52.2	21.3	0.67
HD C–S–H	82.8	26.4	0.99

here that the identified properties are only valid in the current 2D lattice model. The identification results must vary with the uses of different segmentation methods, resolutions, and constitutive laws.

The identified properties for different phases are presented in Table 2. f_i, E_i, and C_i represent tensile strength, elastic modulus, and creep modulus of individual phase, respectively. The mechanical properties of individual phases are found to be quite similar to the results reported in H. Zhang et al. (2016), H. Zhang, Šavija, Xu, and Schlangen (2018), and H. Zhang, Šavija et al. (2019). The

TABLE 3 The summary of simulation and experiment results of mechanical properties for different *w/c* ratios

	Simulation		Experiment (Gan et al., 2020)	
w/c	f_g (MPa)	E_g (GPa)	f_g (MPa)	E_g (GPa)
0.3	31.6 ± 3.2	18.2 ± 0.9	28.0 ± 2.7	19.5 ± 1.5
0.4	23.2 ± 3.3	15.0 ± 1.7	23.3 ± 2.8	16.2 ± 1.9
0.5	19.0 ± 3.5	12.4 ± 2.5	16.9 ± 3.7	10.8 ± 2.5

model with local properties is then used to simulate the mechanical and creep behavior of 27 virtual samples acquired in Section 2.1, which have constant properties in the third direction but different microstructures.

3 | RESULTS

3.1 | Mechanical properties

The simulated global stress–strain curves for 27 virtual specimens under bending load are shown in Figure 9. Note that a smoothening technique was applied to overcome the zig-zag behavior in the post-peak stress–strain responses. The obtained average global strength f_g (maximum stress) and elastic modulus E_g, which is determined by the slope of ascending prepeak curve, are summarized in Table 3, together with the experimental results. The typical fractured pattern can be found in Figure 6. It is apparent that under bending load, the major crack initiates at the weakest location of the upper side of the cantilever beam. With increasing load, the crack gradually propagates through the whole beam section and ultimately leads to the failure.

It can also be seen in Table 3 that the simulation results in terms of strength and elastic modulus, even the corresponding standard deviations, agree well with experimental results. Therefore, the identified mechanical properties of individual phases can be used with confidence for the subsequent creep simulation.

3.2 | Creep properties

The simulated specific basic creep compliance curves for 27 virtual specimens are shown in Figure 10. It can be observed that the specific basic creep compliance increases with increasing *w/c* ratio. The large variations in basic creep compliance curves could be mainly attributed to the different microstructures used in the creep simulations. This is consistent with the experimental results, where the variability of measured creep compliance can also be explained by the selected small sampling volumes of the highly heterogeneous material. It is also found that the simulated global creep compliance function can be satisfactorily fitted by a power-law function (Equation 4) with

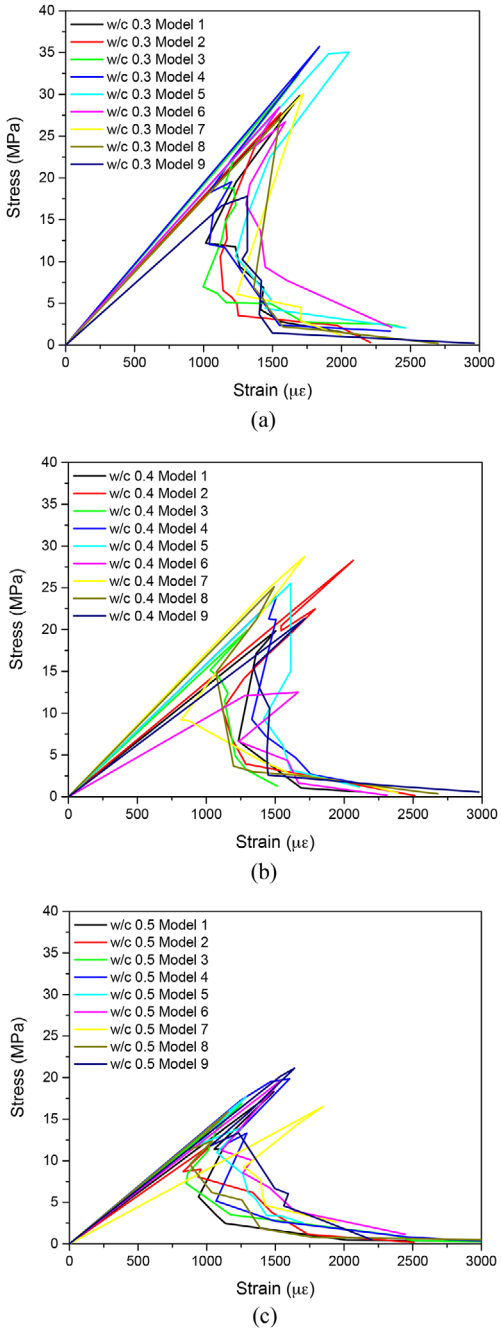

FIGURE 9 The simulated stress–strain responses for (a) *w/c* 0.3, (b) *w/c* 0.4, and (c) *w/c* 0.5

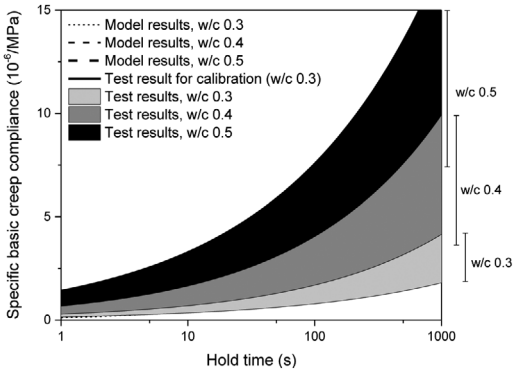

FIGURE 10 Comparison between the numerical and experimental results

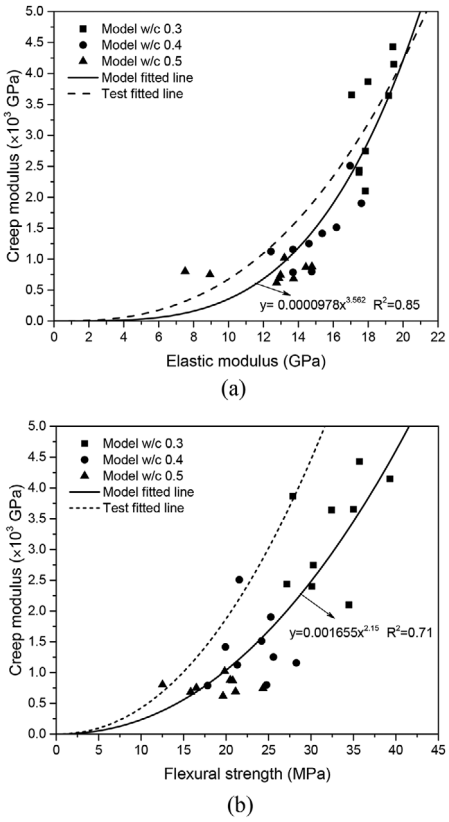

FIGURE 11 Model predicted mechanical properties and creep modulus relationship

an average determination coefficient of 0.99. A constant exponent with a value of 0.33 is also found for all simulated creep functions, which is very close to the experimental results (0.36–0.39) (Gan et al., 2020). Table 4 presents a comparison between the calculated global creep moduli of virtual specimens and the experimental results. The simulated global creep moduli are found to be quite close to the experimental results. Moreover, according to the experimental investigation in Gan et al. (2020), a certain relationship between the global creep modulus and mechanical properties is observed. To examine whether the model can capture this relationship, the simulated mechanical properties, in terms of elastic modulus and strength, are plotted against the global creep modulus in Figure 11. It can be seen that the experimentally obtained relationship is also confirmed by this model. Therefore, the combined fracture and creep models are believed to be validated.

4 | DISCUSSION

It is well known that several microstructural features, such as the volume fractions, morphologies and spatial distributions of different constituents, are crucial for the global behavior of cement paste (Lavergne et al., 2015). However, it is difficult and inefficient to quantify their effects in experiments. Alternatively, the microstructure-informed lattice model could be a potential tool in this aspect.

As pores are usually considered as stress concentration sites and promote failure under loading, the porosity is regarded as the governing factor, among all microstructural features, for the fracture strength of porous materials (B. Pichler et al., 2013; H. Zhang et al., 2018). The relationships between the porosity and mechanical properties of virtual specimens are shown in Figure 12. These relationships can be well predicted with the empirical formulas developed for porous materials (Duckworth, 1953; Spriggs, 1961). It is clear that the flexural strength increases with the decreasing porosity. In addition, large variations of simulation results are observed. Unlike in the experiments, where the encountered shrinkage, damage, and carbonation may increase the uncertainty of results, the only variable considered in the current model is the microstructure. Therefore, the observed scatters in Figure 12 are only caused by the heterogeneity of microstructure. Note that due to the nonuniform stresses inside the beam under flexural loading, the spatial dis-

TABLE 4 The summary of simulation and experiment results of creep functions for different *w/c* ratios

	Simulation		Experiment (Gan et al., 2020)	
w/c	C_g ($\times 10^3$ GPa)	β_g	C_g ($\times 10^3$ GPa)	β_g
0.3	3.42 ± 0.78	0.33	4.38 ± 0.72	0.39
0.4	1.40 ± 0.29	0.33	1.98 ± 0.33	0.39
0.5	0.78 ± 0.14	0.33	0.88 ± 0.22	0.36

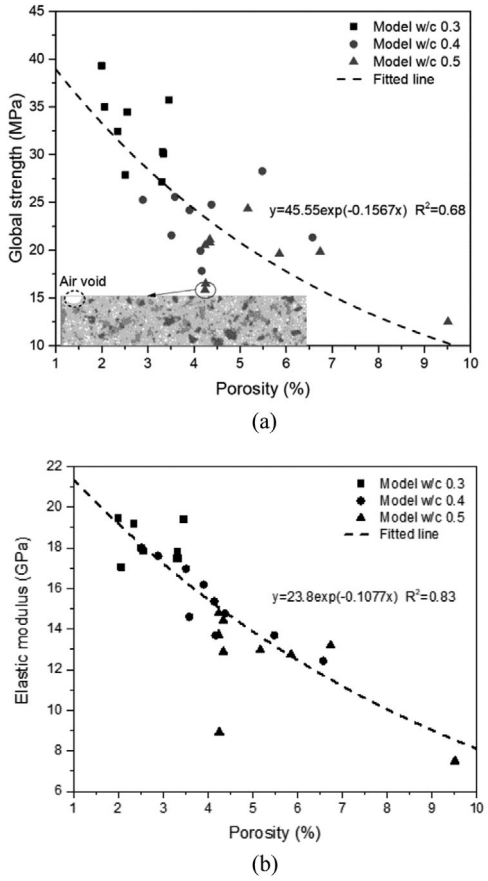

FIGURE 12 Relationship between the mechanical properties and porosity

tribution of pores and hydration products becomes more important compared to the uniaxial compressive/tensile loading (Gan et al., 2018). For instance, the increased local porosity at the fixed end of beam largely reduces the global strength even with similar overall porosity as shown in Figure 12a. Furthermore, it should be highlighted that the scatter of 2D simulation is expected to be larger compared to the 3D simulation, as irregularities, like air voids, are averaged out in the 3D simulation. With respect to the elastic modulus, the capillary porosity also plays a dominant role, but the elastic modulus seems to be less sensitive to the spatial distribution of hydration products if the porosity is the same. This is supported by directly checking the microstructure of virtual specimens, which are not presented here, and indirect evidence of higher determination coefficient. It should be mentioned that in addition to the porosity and hydration products, the volume fractions and distributions of UHC grains may also affect the overall mechanical properties (B. Pichler et al., 2013; H. Zhang et al., 2016). Herein, only their effects on the global creep behavior of cement paste will be discussed later.

The identification of viscoelastic properties of C–S–H phases at finer scale (5 μm) is achieved through inverse analysis from the cement paste scale. The identified creep behaviors of two types of C–S–H are described using a single power-law creep function (Z. Hu, Hilaire, Wyrzykowski, Lura, & Scrivener, 2020; Irfan-ul-Hassan, Pichler, Reihsner, & Hellmich, 2016; Tamtsia & Beaudoin, 2000). Similarly, it has been reported in Königsberger et al. (2016) that upscaling of a short-term power-law creep function from needle-shaped hydrates up to the scale of cement paste also results in a power-law creep function. In other words, the shape of the creep function will not be altered by the transition of scales (Šmilauer & Bažant, 2010). This is also found for the upscaling of long-term logarithmic creep function of C–S–H identified by nanoindentation creep tests up to larger scales (Do, Bishnoi, & Scrivener, 2016; C. Pichler & Lackner, 2009). For the identified creep modulus, the C–S–H phases in this model are actually composed of C–S–H gel and small pores. The difference in local creep properties between LD and HD C–S–H is therefore assumed to be mainly caused by the different gel porosities (Vandamme & Ulm, 2009). In addition, during the segmentation process, other elastic phases, for example, CH and AFt, are not explicitly considered. Therefore, the identified creep moduli of C–S–H phases are actually higher than the pure C–S–H phase. In addition, if C–S–H phases experience significant heating, drying, or aging, for example, hydration-induced microstructure modification or silicate polymerization at C–S–H level (Bažant et al., 1997; Di Luzio & Cusatis, 2013; Do et al., 2016; Giorla & Dunant, 2018; Granger & Bažant, 1995; Masoero, Cusatis, & Di Luzio, 2018), the creep functions for C–S–H must vary relative to the temperature, humidity, or age. Therefore, in this context, the nonaging (time-invariant) viscoelasticity of C–S–H phase for the case of no temperature and moisture change is identified by the current model.

It is well acknowledged that the properties of C–S–H gel in terms of nanostructure and moisture content may vary with the *w*/*c* ratio and chemical composition of raw material (Foley, Kim, & Reda Taha, 2012; C. Hu & Li, 2014). Dependence of viscoelastic properties of C–S–H gel on material composition has also been confirmed in nanoindentation creep tests (Vandamme & Ulm, 2013). This seems to be contradicted with the basic assumption in current study, which presumes that the C–S–H phases with different *w*/*c* ratios (0.3–0.5) exhibit similar creep properties. However, it has been recently argued by Z. Hu et al. (2019) that the apparent differences observed in the macroscopic creep compliance of various cement-based systems prepared with different *w*/*c* (0.35–0.63) could be mainly explained by their different capillary porosities and solid volume fractions at the cement paste level. This means that with respect to the influence on the macroscopic creep of cement paste, the change of microstructure due

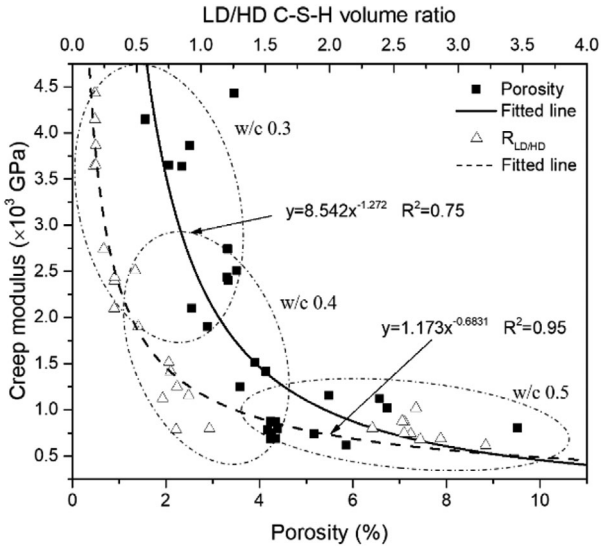

FIGURE 13 The variation of creep modulus with the porosity and the LD/HD C–S–H volume ratio

to the varying of *w*/*c* ratio is more pronounced compared to the change of nanostructure. Pursuing this argument to the scale of concrete, one can also anticipate that several mesostructural features, such as the content of aggregates and the incorporation of ITZ, may dominate the macroscopic creep behavior of concrete. Note that this statement appears to be true within the investigated *w*/*c* ratio range in this study. Nevertheless, caution should be taken if the material composition differs largely (C. Hu & Li, 2014, 2015).

The focus is now fixed on the microstructural effect on the creep of cement paste. It is clear that the increase of *w*/*c* ratio leads to a higher creep compliance of cement paste, as shown in Table 4. From the microstructure perspective, given the same age of paste (28 days), the increase of *w*/*c* ratio results in an increase in capillary porosity, higher LD/HD C–S–H volume ratio, and also lower volume fraction of UHC. When subjected to the same external stress, the creeping phases would sustain higher stress as a result of increased porosity. In addition, because the UHC mainly acts as elastic restraint in the cement paste, higher creep would be expected when there is less UHC in the system. Therefore, all these resultant microstructural features due to the increase of *w*/*c* ratio lead to the reduction of global creep modulus.

To check the predominance of microstructural factors, the global creep modulus is plotted as a function of LD/HD C–S–H volume ratio and porosity in Figure 13. Even though a general decreasing trend of creep modulus with the porosity is observed in Figure 13, it is known that the porosity is not the sole factor accounting for this trend as mentioned above. Note that the porosities are only around 1–9% of total volume in the virtual specimens, their effects on the global creep modulus are limited. Consequently, for a given *w*/*c* ratio, the apparent dependence of the creep modulus on the porosity is not evident. This statement also holds for the UHC as very low volume fractions of UHC are included in the microstructures. Instead, a good correlation is observed between the volume ratio of LD/HD C–S–H and the creep modulus indicated by the high determination coefficient. It seems reasonable as the total hydration products, LD/HD C–S–H in this case, account for around 80% volume of the microstructure for three *w*/*c* ratios, the global creep modulus is mainly dependent on the compositions of two types of C–S–H. It should be mentioned here that the deduction may be biased as the role of CH is ignored in the simulations. Nevertheless, it has been reported in Z. Hu et al. (2019), Mounanga, Khelidj, Loukili, and Baroghel-Bouny (2004), Ye (2003), and H. Zhang, Rodriguez et al. (2020) that there is a very small difference for the amount of CH in mature cement pastes with different *w*/*c* ratios. Therefore, the statement regarding the governing effects of the LD/HD C–S–H volume fractions on global creep modulus remains unaffected. Moreover, because the LD C–S–H contains higher gel porosity than HD C–S–H (Tennis & Jennings, 2000), the increased volume fraction of LD C–S–H essentially leads to higher total porosity in the microstructure and thus to a lower creep modulus. The spatial distributions and morphologies of phases in the microstructure may also affect the global creep behavior to some extent (Giorla & Dunant, 2018; Lavergne et al., 2015) and they can also be properly investigated using the current lattice model, but these effects are not presented in this study.

In future study, the extension of the current model to account for more complex phenomena, such as the interactions with microcracking, evolution of microstructure due to hydration and drying process, will be explored. These effects could be investigated by combining with the existing lattice fracture model (Lilliu & van Mier, 2003; H. Zhang, Gan et al., 2019), hydration model (Van Breugel, 1993), as well as the moisture transport lattice model (Luković et al., 2016; Šavija et al., 2014). Moreover, the multiscale modeling scheme developed in H. Zhang et al. (2017) and H. Zhang, Xu, Gan, Schlangen, and Šavija (2020) allows us to predict the creep behavior of mortar or concrete at the meso- and macroscale. The outcome of creep simulations of cement paste at the microscale, which considers the effects of microstructures resulted from different mixtures, will be used to determine the constitutive properties in the simulations of concrete at the mesoscale (Giorla & Dunant, 2018; H. Zhang, Gan et al., 2019).

5 | CONCLUSION

The original contributions of current study include the extension of lattice model to simulate the creep behavior of cement paste at the microscale, the identification of local creep properties for different constituents at the resolution of 5 μm and the direct validation of the model at the microscale combined with the experimental results. The estimation of microstructural effect on macroscopic creep response of cement paste was also performed using the developed model. This is the first attempt to develop and directly validate such a lattice creep model at the microscale, which is also an essential starting point in the development of multiscale modeling scheme for predicting creep of concrete structure. Several conclusions can be drawn from the numerical investigations:

- The experimentally informed lattice creep model developed in this study has the clear advantage in considering the realistic microstructure and is able to properly explain the experimental results. Moreover, both fracture and creep models can successfully reproduce the experimentally observed behaviors.
- The constitutive properties of different phases, including mechanical and creep properties, were identified based on the microscale tests of cement paste through the back analysis. The assumption that the identified properties at the scale of 5 μm are not largely affected by the w/c ratios seems to be appropriate in the current study. With these identified properties and the developed model, it would be possible to predict the short-term creep of any cement paste given the microstructure.
- In this study, the creep numerical analysis is converted into a sequence of fictitious elasticity problems with imposed local forces and solved with the help of the finite-element method. The developed numerical procedure requires no approximation of the creep constitutive law. Assumed single power-law creep functions for LD C–S–H and HD C–S–H, which make the numerical evaluation straightforward and efficient, are believed to give satisfactory results in simulating the short-term creep behavior of mature cement paste.
- The developed model can also help to establish the relationship between the microstructural features and the macroscopic creep properties. This is also an essential starting point for the development of multiscale modeling scheme for predicting creep of concrete structure.
- According to the simulation analysis, it is suggested that the variation of global creep compliance of cement paste prepared with different w/c ratios can be mainly explained by the different volume ratios between the LD C–S–H and HD C–S–H. The lower global creep modulus observed for higher volume fraction of LD C–S–H is essentially caused by the increased porosity embedded in the LD C–S–H.
- A major limitation of the current model is its 2D nature. It is important and necessary to perform 3D simulation in future study. Generally, the developed model is simple to implement and gives comparable results with experiments. Further development could also focus on including more complex phenomena (such as shrinkage and aging) and upscaling the microscopic creep behavior of cement paste to the creep behavior of concrete at the macroscale.

ACKNOWLEDGMENTS

Yidong Gan would like to acknowledge the funding supported by China Scholarship Council under grant number 201706130140. Claudia Romero Rodriguez acknowledges the financial support from the Construction Technology Research Program funded by the Ministry of Land, Infrastructure and Transport of the Korean Government under the grant 17SCIP-B103706-03. Hongzhi Zhang acknowledges the financial support from the Taishan Scholar Foundation of Shandong Province under the grant number tsqn201909032.

REFERENCES

Alizadeh, R., Beaudoin, J. J., & Raki, L. (2010). Viscoelastic nature of calcium silicate hydrate. *Cement and Concrete Composites*, *32*(5), 369–376.

Bažant, Z. P. (1971). Numerically stable algorithm with increasing time steps for integral-type ageing creep. *Proceedings of the 1st International Conference on Structural Mechanics in Reactor Technology, Berlin*.

Bažant, Z. P. (1972). Numerical determination of long-range stress history from strain history in concrete. *Matériaux et Constructions*, *5*(3), 135–141.

Bažant, Z. P. (1988). *Mathematical modeling of creep and shrinkage of concrete*. New York: Wiley.

Bažant, Z. P., Hauggaard, A. B., Baweja, S., & Ulm, F. J. (1997). Microprestress-solidification theory for concrete creep. I: Aging and drying effects. *Journal of Engineering Mechanics*, *123*(11), 1188–1194.

Bažant, Z. P., Hubler, M. H., & Yu, Q. (2011). Pervasiveness of excessive segmental bridge deflections: Wake-up call for creep. *ACI Structural Journal*, *108*(6), 766–774.

Bažant, Z. P., & Prasannan, S. (1989). Solidification theory for concrete creep. II: Verification and application. *Journal of Engineering Mechanics*, *115*(8), 1704–1725.

Beltempo, A., Bursi, O. S., Cappello, C., Zonta, D., & Zingales, M. (2018). A viscoelastic model for the long-term deflection of segmental prestressed box girders. *Computer-Aided Civil and Infrastructure Engineering*, *33*(1), 64–78.

Bentz, D. P. (2006). Modeling the influence of limestone filler on cement hydration using CEMHYD3D. *Cement and Concrete Composites*, *28*(2), 124–129.

Bishnoi, S., & Scrivener, K. L. (2009). μic: A new platform for modelling the hydration of cements. *Cement and Concrete Research*, *39*(4), 266–274.

Bolander, J. E., & Berton, S. (2004). Simulation of shrinkage induced cracking in cement composite overlays. *Cement and Concrete Composites*, *26*(7), 861–871.

Constantinides, G., & Ulm, F. J. (2004). The effect of two types of C-S-H on the elasticity of cement-based materials: Results from nanoindentation and micromechanical modeling. *Cement and Concrete Research*, *34*(1), 67–80.

Di Luzio, G., Cedolin, L., & Beltrami, C. (2020). Tridimensional long-term finite element analysis of reinforced concrete structures with rate-type creep approach. *Applied Sciences*, *10*(14), 1–36.

Di Luzio, G., & Cusatis, G. (2013). Solidification-microprestress-microplane (SMM) theory for concrete at early age: Theory, validation and application. *International Journal of Solids and Structures*, *50*(6), 957–975.

Do, Q. H., Bishnoi, S., & Scrivener, K. L. (2016). Microstructural modeling of early-age creep in hydrating cement paste. *Journal of Engineering Mechanics*, *142*(11), 04016086.

Duckworth, W. (1953). Discussion of Ryshkewitch paper by Winston Duckworth. *Journal of the American Ceramic Society*, *36*(2), 68–68.

Foley, E. M., Kim, J. J., & Reda Taha, M. M. (2012). Synthesis and nano-mechanical characterization of calcium-silicate-hydrate (C-S-H) made with 1.5 CaO/SiO_2 mixture. *Cement and Concrete Research*, *42*(9), 1225–1232.

Forth, J. P. (2015). Predicting the tensile creep of concrete. *Cement and Concrete Composites*, *55*, 70–80.

Gan, Y., Vandamme, M., Zhang, H., Chen, Y., Schlangen, E., van Breugel, K., & Šavija, B. (2020). Micro-cantilever testing on the short-term creep behaviour of cement paste at micro-scale. *Cement and Concrete Research*, *134*, 1–26.

Gan, Y., Zhang, H., Šavija, B., Schlangen, E., & van Breugel, K. (2018). Static and fatigue tests on cementitious cantilever beams using nanoindenter. *Micromachines*, *9*, 630.

Gawin, D., Pesavento, F., & Schrefler, B. A. (2006). Hygro-thermo-chemo-mechanical modelling of concrete at early ages and beyond. Part II: Shrinkage and creep of concrete. *International Journal for Numerical Methods in Engineering*, *67*(3), 332–363.

Giorla, A. B., & Dunant, C. F. (2018). Microstructural effects in the simulation of creep of concrete. *Cement and Concrete Research*, *105*, 44–53.

Granata, M. F., Margiotta, P., & Arici, M. (2013). Simplified procedure for evaluating the effects of creep and shrinkage on prestressed concrete girder bridges and the application of European and North American prediction models. *Journal of Bridge Engineering*, *18*(12), 1281–1297.

Granger, L. P., & Bažant, Z. P. (1995). Effect of composition on basic creep of concrete and cement paste. *Journal of Engineering Mechanics*, *121*(11), 1261–1270.

Havlásek, P., & Jirásek, M. (2016). Multiscale modeling of drying shrinkage and creep of concrete. *Cement and Concrete Research*, *85*, 55–74.

Honorio, T., Bary, B., & Benboudjema, F. (2016). Multiscale estimation of ageing viscoelastic properties of cement-based materials: A combined analytical and numerical approach to estimate the behaviour at early age. *Cement and Concrete Research*, *85*, 137–155.

Hu, C., & Li, Z. (2014). Micromechanical investigation of Portland cement paste. *Construction and Building Materials*, *71*, 44–52.

Hu, C., & Li, Z. (2015). A review on the mechanical properties of cement-based materials measured by nanoindentation. *Construction and Building Materials*, *90*, 80–90.

Hu, Z., Hilaire, A., Ston, J., Wyrzykowski, M., Lura, P., & Scrivener, K. (2019). Intrinsic viscoelasticity of C-S-H assessed from basic creep of cement pastes. *Cement and Concrete Research*, *121*, 11–20.

Hu, Z., Hilaire, A., Wyrzykowski, M., Lura, P., & Scrivener, K. (2020). Visco-elastic behavior of blended cement pastes at early ages. *Cement and Concrete Composites*, *107*, 103497.

Huang, Y., Yan, D., Yang, Z., & Liu, G. (2016). 2D and 3D homogenization and fracture analysis of concrete based on in-situ X-ray computed tomography images and Monte Carlo simulations. *Engineering Fracture Mechanics*, *163*, 37–54.

Irfan-Ul-Hassan, M., Pichler, B., Reihsner, R., & Hellmich, C. (2016). Elastic and creep properties of young cement paste, as determined from hourly repeated minute-long quasi-static tests. *Cement and Concrete Research*, *82*, 36–49.

Jones, C. A., & Grasley, Z. C. (2011). Short-term creep of cement paste during nanoindentation. *Cement and Concrete Composites*, *33*(1), 12–18.

Königsberger, M., Irfan-ul-Hassan, M., Pichler, B., & Hellmich, C. (2016). Downscaling based identification of nonaging power-law creep of cement hydrates. *Journal of Engineering Mechanics*, *142*(12), 1–11.

Lavergne, F., Sab, K., Sanahuja, J., Bornert, M., & Toulemonde, C. (2015). Investigation of the effect of aggregates' morphology on concrete creep properties by numerical simulations. *Cement and Concrete Research*, *71*, 14–28.

Li, X., Grasley, Z. C., Garboczi, E. J., & Bullard, J. W. (2015). Modeling the apparent and intrinsic viscoelastic relaxation of hydrating cement paste. *Cement and Concrete Composites*, *55*, 322–330.

Liang, S., & Wei, Y. (2019). Methodology of obtaining intrinsic creep property of concrete by flexural deflection test. *Cement and Concrete Composites*, *97*, 288–299.

Lilliu, G., & van Mier, J. G. M. (2003). 3D lattice type fracture model for concrete. *Engineering Fracture Mechanics*, *70*(7–8), 927–941.

Luković, M., Šavija, B., Schlangen, E., Ye, G., & van Breugel, K. (2016). A 3D lattice modelling study of drying shrinkage damage in concrete repair systems. *Materials*, *9*(7), 9–13.

Luković, M., Schlangen, E., & Ye, G. (2015). Combined experimental and numerical study of fracture behaviour of cement paste at the microlevel. *Cement and Concrete Research*, *73*, 123–135.

Lyu, W., Schlangen, E., & van Breugel, K. (2018). Numerical analysis of effect of micro-cracking and selfhealing on the long-term creep of cementitious materials. *Proceedings of the Symposium on Concrete Modelling: CONMOD2018 August 27–30, Delft, the Netherlands. Paris*: RILEM.

Mallick, S., Anoop, M. B., & Balaji Rao, K. (2019). Early age creep of cement paste—Governing mechanisms and role of water—A microindentation study. *Cement and Concrete Research*, *116*, 284–298.

Masoero, E., Cusatis, G., & Di Luzio, G. (2018). C–S–H gel densification: The impact of the nanoscale on self-desiccation and sorption isotherms. *Cement and Concrete Research*, *109*, 103–119.

Moradian, M., Ley, M. T., & Grasley, Z. C. (2018). Stress induced dissolution and time-dependent deformation of Portland cement paste. *Materials and Design*, *157*, 314–325.

Mounanga, P., Khelidj, A., Loukili, A., & Baroghel-Bouny, V. (2004). Predicting $Ca(OH)_2$ content and chemical shrinkage of hydrating cement pastes using analytical approach. *Cement and Concrete Research*, *34*(2), 255–265.

Park, Y. S., Lee, Y. H., & Lee, Y. (2016). Description of concrete creep under time-varying stress using parallel creep curve. *Advances in Materials Science and Engineering*, *2016*. https://doi.org/10.1155/2016/9370514

Pichler, B., & Hellmich, C. (2011). Upscaling quasi-brittle strength of cement paste and mortar: A multi-scale engineering mechanics model. *Cement and Concrete Research*, *41*(5), 467–476.

Pichler, B., Hellmich, C., Eberhardsteiner, J., Wasserbauer, J., Termkhajornkit, P., Barbarulo, R., & Chanvillard, G. (2013). Effect of gel-space ratio and microstructure on strength of hydrating cementitious materials: An engineering micromechanics approach. *Cement and Concrete Research*, *45*(1), 55–68.

Pichler, C., & Lackner, R. (2009). Identification of logarithmic-type creep of calcium-silicate-hydrates by means of nanoindentation. *Strain*, *45*(1), 17–25.

Qian, Z. (2012). *Multiscale modeling of fracture processes in cementitious materials* (PhD thesis). Alblasserdam: Haveka.

Rahimi-Aghdam, S., Bažant, Z. P., & Cusatis, G. (2019). Extended microprestress-solidification theory for long-term creep with diffusion size effect in concrete at variable environment. *Journal of Engineering Mechanics*, *145*(2), 1–14.

Ranaivomanana, N., Multon, S., & Turatsinze, A. (2013). Tensile, compressive and flexural basic creep of concrete at different stress levels. *Cement and Concrete Research*, *52*, 1–10.

Rossi, P., Tailhan, J. L., & Le Maou, F. (2013). Comparison of concrete creep in tension and in compression: Influence of concrete age at loading and drying conditions. *Cement and Concrete Research*, *51*, 78–84.

Rossi, P., Tailhan, J. L., Le Maou, F., Gaillet, L., & Martin, E. (2012). Basic creep behavior of concretes investigation of the physical mechanisms by using acoustic emission. *Cement and Concrete Research*, *42*(1), 61–73.

Sassone, M., & Casalegno, C. (2012). Evaluation of the structural response to the time-dependent behaviour of concrete: Part 2—A general computational approach. *Indian Concrete Journal*, *86*(12), 25–36.

Šavija, B., Luković, M., & Schlangen, E. (2014). Lattice modeling of rapid chloride migration in concrete. *Cement and Concrete Research*, *61–62*, 49–63.

Šavija, B., Zhang, H., & Schlangen, E. (2020). Micromechanical testing and modelling of blast furnace slag cement pastes. *Construction and Building Materials*, *239*, 117841.

Schlangen, E., & Garboczi, E. J. (1997). Fracture simulations of concrete using lattice models: Computational aspects. *Engineering Fracture Mechanics*, *57*(2–3), 319–332.

Schlangen, E., & van Mier, J. G. M. (1992). Simple lattice model for numerical simulation of fracture of concrete materials and structures. *Materials and Structures*, *25*(9), 534–542.

Sellier, A., Multon, S., Buffo-Lacarrière, L., Vidal, T., Bourbon, X., & Camps, G. (2016). Concrete creep modelling for structural applications: Non-linearity, multi-axiality, hydration, temperature and drying effects. *Cement and Concrete Research*, *79*, 301–315.

Shahrin, R., & Bobko, C. P. (2019). Micropillar compression investigation of size effect on microscale strength and failure mechanism of calcium-silicate-hydrates (C-S-H) in cement paste. *Cement and Concrete Research*, *125*, 105863.

Šmilauer, V., & Bažant, Z. P. (2010). Identification of viscoelastic C-S-H behavior in mature cement paste by FFT-based homogenization method. *Cement and Concrete Research*, *40*, 197–207.

Spriggs, R. M. (1961). Expression for effect of porosity on elastic modulus of polycrystalline refractory materials, particularly aluminum oxide. *Journal of the American Ceramic Society*, *44*(12), 628–629.

Suwanmaneechot, P., Aili, A., & Maruyama, I. (2020). Creep behavior of C-S-H under different drying relative humidities: Interpretation of microindentation tests and sorption measurements by multiscale analysis. *Cement and Concrete Research*, *132*, 106036.

Tamtsia, B. T., & Beaudoin, J. J. (2000). Basic creep of hardened cement paste. A re-examination of the role of water. *Cement and Concrete Research*, *30*(9), 1465–1475.

Tennis, P. D., & Jennings, H. M. (2000). A model for two types of calcium silicate hydrate in the microstructure of Portland cement pastes. *Cement and Concrete Research*, *30*(6), 855–863.

Van Breugel, K. (1993). *Simulation of hydration and formation of structure in hardening cement-based materials*. Delft: Delft University Press.

Vandamme, M., & Ulm, F. J. (2009). Nanogranular origin of concrete creep. *Proceedings of the National Academy of Sciences of the United States of America*, *106*(26), 10552–10557.

Vandamme, M., & Ulm, F. J. (2013). Nanoindentation investigation of creep properties of calcium silicate hydrates. *Cement and Concrete Research*, *52*, 38–52.

Vichit-Vadakan, W., & Scherer, G. W. (2003). Measuring permeability and stress relaxation of young cement paste by beam bending. *Cement and Concrete Research*, *33*(12), 1925–1932.

Wei, Y., Wu, Z., Huang, J., & Liang, S. (2018). Comparison of compressive, tensile, and flexural creep of early-age concretes under sealed and drying conditions. *Journal of Materials in Civil Engineering*, *30*(11), 1–13.

Wittmann, F. H. (1982). Creep and shrinkage mechanisms. In *Creep and shrinkage in* concrete structures (pp. 129–161). Chichester: Wiley.

Wong, H. S., Head, M. K., & Buenfeld, N. R. (2006). Pore segmentation of cement-based materials from backscattered electron images. *Cement and Concrete Research*, *36*(6), 1083–1090.

Wyrzykowski, M., Scrivener, K., & Lura, P. (2019). Basic creep of cement paste at early age—The role of cement hydration. *Cement and Concrete Research*, *116*, 191–201.

Ye, G. (2003). *Experimental study and numerical simulation of the development of the microstructure and permeability of cementitious materials*. Delft: Delft University Press.

Yip, M., Mohle, J., & Bolander, J. E. (2005). Automated modeling of three-dimensional structural components using irregular lattices. *Computer-Aided Civil and Infrastructure Engineering*, *20*(6), 393–407.

Yu, P., Duan, Y. H., Chen, E., Tang, S. W., Hanif, A., & Fan, Y. L. (2018). Microstructure-based homogenization method for early-age creep of cement paste. *Construction and Building Materials*, *188*, 1193–1206.

Zhang, H., Gan, Y., Xu, Y., Zhang, S., Schlangen, E., & Šavija, B. (2019). Experimentally informed fracture modelling of interfacial transition zone at micro-scale. *Cement and Concrete Composites*, 104, 103383.

Zhang, H., Rodriguez, C. R., Dong, H., Gan, Y., Schlangen, E., & Šavija, B. (2020). Elucidating the effect of accelerated carbonation on porosity and mechanical properties of hydrated Portland cement paste using X-ray tomography and advanced micromechanical testing. *Micromachines*, *11*(5), 471.

Zhang, H., Šavija, B., Figueiredo, S. C., Lukovic, M., & Schlangen, E. (2016). Microscale testing and modelling of cement paste as basis for multi-scale modelling. *Materials*, *9*(11), 907.

Zhang, H., Šavija, B., Figueiredo, S. C., & Schlangen, E. (2017). Experimentally validated multi-scale modelling scheme of deformation and fracture of cement paste. *Cement and Concrete Research*, *102*, 175–186.

Zhang, H., Šavija, B., Luković, M., & Schlangen, E. (2019). Experimentally informed micromechanical modelling of cement paste: An approach coupling X-ray computed tomography and statistical nanoindentation. *Composites Part B: Engineering*, *157*, 109–122.

Zhang, H., Šavija, B., & Schlangen, E. (2018). Towards understanding stochastic fracture performance of cement paste at micro length scale based on numerical simulation. *Construction and Building Materials*, *183*, 189–201.

Zhang, H., Šavija, B., Xu, Y., & Schlangen, E. (2018). Size effect on splitting strength of hardened cement paste: Experimental and numerical study. *Cement and Concrete Composites*, *94*, 264–276.

Zhang, H., Xu, Y., Gan, Y., Schlangen, E., & Šavija, B. (2020). Experimentally validated meso-scale fracture modelling of mortar using output from micromechanical models. *Cement and Concrete Composites*, 110, 103383.

Zhang, M., He, Y., Ye, G., Lange, D. A., & van Breugel, K. (2012). Computational investigation on mass diffusivity in Portland cement paste based on X-ray computed microtomography (μCT) image. *Construction and Building Materials*, *27*(1), 472–481.

Zhang, Q., Le Roy, R., Vandamme, M., & Zuber, B. (2014). Long-term creep properties of cementitious materials: Comparing microindentation testing with macroscopic uniaxial compressive testing. *Cement and Concrete Research*, *58*, 89–98.

How to cite this article: Gan Y, Romero Rodriguez C, Zhang H, Schlangen E, van Breugel K, Šavija B. Modeling of microstructural effects on the creep of hardened cement paste using an experimentally informed lattice model. *Comput Aided Civ Inf*. 2021;*36*:560–576. https://doi.org/10.1111/mice.12659